IET Power Electronics

Research Article

Cascaded full-bridge resonant inverter configuration for different material vessel induction cooking

ISSN 1755-4535
Received on 17th June 2020
Revised 18th November 2020
Accepted on 10th December 2020
E-First on 28th January 2021
doi: 10.1049/iet-pel.2020.0728
www.ietdl.org

Srinivas Khatroth[1] ✉, Porpandiselvi Shunmugam[1]
[1]Department of Electrical Engineering, National Institute of Technology, Warangal, TS, India
✉ *E-mail: srinukhitu@student.nitw.ac.in*

Abstract: This paper presents a cascaded full-bridge resonant inverter configuration for different material vessel induction cooking. The proposed inverter configuration features simultaneous heating of three different material vessels, and independent power control. In this proposed work, three different induction heating loads are simultaneously operated at their respective resonant frequencies. Vessels of iron, steel, and aluminium materials are used. The output powers are independently controlled by an asymmetric duty cycle control. The proposed inverter is designed and hardware prototype has been implemented. Experimental results are validated with simulation results.

1 Introduction

The induction heating (IH) technology is growing progressively with domestic, medical, and industrial applications [1–3]. Induction heating technologies have many advantages over resistive heating, microwave ovens, flame heating, or furnaces. Some of the benefits are cleanliness, fast heating, safety, and efficient control.

In induction heating, a high frequency magnetic field is produced around the object to be heated. It produces high frequency eddy current into the object. If the material is ferromagnetic, then both hysteresis loss and eddy current loss are causing the heat generation. If the material is non-ferromagnetic, then heat generation is based on eddy current loss only. Most of the IH converter topologies are based on high-frequency resonant inverter configurations.

In the literature, different inverter topologies have been proposed for IH, such as single switch [4], half-bridge [5], and full-bridge resonant inverters [6, 7]. In these inverter topologies different power regulation schemes like, pulse-width modulation [8], pulse-frequency modulation [9], asymmetric voltage cancellation [10], asymmetric duty cycle control (ADC) [11], phase shift control [12], and pulse-density modulation [13] are used. All these power regulation schemes have their own merits and demerits.

Nowadays, multiple-load induction cooking (IC) systems are becoming more popular. The main requirements of this system are reduced component count, improved conversion efficiency, and independent power regulation of loads. In the past, some inverter topologies have been proposed for multiple load induction heating. In [14], a multi-output inverter configuration with variable frequency control is proposed. Electromechanical switches are used. An inverter topology with three legs is proposed in [15] for powering two loads with one leg is common for both loads. In [16], a multi-output inverter with independent on–off control is proposed. In [17], a multiple load inverter with dual-frequency operation is proposed. The ADC control technique is used for independent power control of each load. In [18], a boost resonant ac–ac converter is proposed for multiple-output. In [19], a matrix converter is proposed for multiple-load IH systems. It has more component count and complex control. Most of the proposed multi-output IH inverter topologies are suffering from one or many of the following limitations: the use of electro-mechanical switches, several combinations of resonant capacitors obtained through electro-mechanical switches, lack of independent power control, lack of accuracy in independent control, complex control, etc.

Most of the available multi-load IH configurations are suitable for ferromagnetic materials only. However, non-ferromagnetic vessels such as aluminium and copper cannot be used with the IC, though they are having good thermal properties and are commonly used in cooking applications. In the recent past, some inverter configurations suitable for vessels made from ferro and non-ferro magnetic materials, have been proposed. In [20, 21], a time-sharing high frequency resonant inverter is proposed for all metal induction heating applications. In [22, 23], double induction coil-based inverter topologies are proposed. In [24], a modified half-bridge topology with selective harmonic operation is proposed. In [25], a series resonant, load adaptive control-based converter is proposed. In all these inverter configurations, electro-mechanical switches are used to select the resonant capacitor combinations or induction coil, which is their major limitation.

In the literature, cascaded multi-level inverter topologies [26–32] are proposed for different applications like photovoltaic, AC power distribution and industrial applications. In these configurations, cascaded bridges are operated at single frequency to supply single load. Different modulation control techniques are used for load power control. In [33–36], cascaded multi-level inverter configurations have been proposed for induction heating applications. In [33, 34], dual-frequency multilevel inverter topology has been proposed with equal and unequal voltage sources. In [35], a cascaded multi-level inverter topology has been proposed for high-power induction heating application. These cascaded inverter configurations have been proposed for the single ferro magnetic induction heating loads [36], the cascaded inverter topology has been proposed for an induction hardening application. These proposed multi-level inverter configurations have their own merits and demerits.

In this paper, a cascaded full-bridge resonant inverter configuration, which is suitable for three different material vessels, has been proposed. It can power multiple-loads of iron, steel, and aluminium vessels. These three IH loads are simultaneously operated at their respective resonant frequencies. The output power of multiple loads is independently controlled by an asymmetric duty cycle control. This configuration provides advantages of a reduced component count, high efficiency, and independent control. The block diagram of the proposed inverter configuration is shown in (Fig. 1). The outputs of two full-bridge inverters are cascaded and connected to three IH resonant loads. The first inverter is operated at low and medium frequencies suitable for iron and steel loads. The second inverter is operated at high

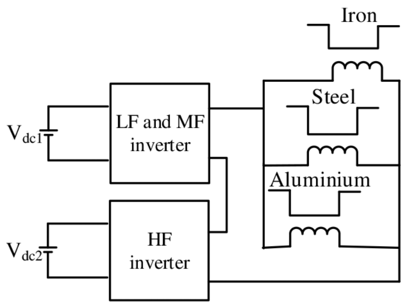

Fig. 1 *Block diagram of cascaded multi-load inverter for induction cooking*

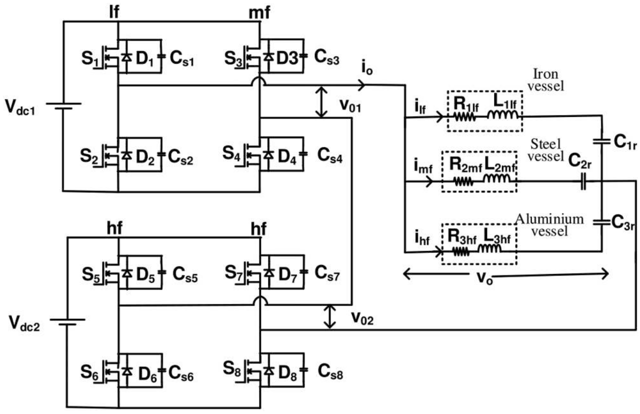

Fig. 2 *Proposed cascaded multi-load inverter configuration*

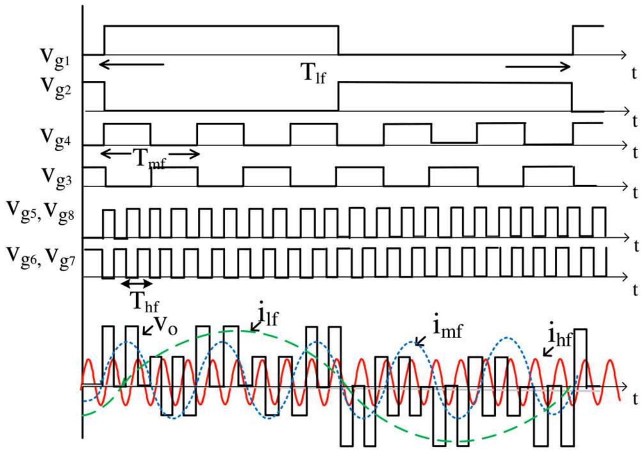

Fig. 3 *Switching pulses, output voltage, and load currents*

frequency suitable for aluminium loads. The ADC control is used for an output power control. Circuit operation, design, implementation, and result analysis are presented in the following sections.

This paper is organised as follows. In Section 2, proposed circuit configuration and principle of operation are described. Section 3 presents different modes of operation. Section 4 describes prototype implementation, simulation, and experimental results. Analysis of results is presented in Section 5. Section 6 summarises this paper and concludes.

2 Proposed cascaded converter configuration

2.1 Circuit configuration

The circuit diagram of the proposed multi-load inverter topology is shown in (Fig. 2). This configuration consists of two full-bridge inverters connected in a cascade. S_1 to S_4 are the four MOSFET switches of the first inverter with body diodes D_1 to D_4 and snubber capacitors C_{S1} to C_{S4}, respectively. The first leg devices S_1 and S_2 are switched at low frequency, f_l. The second leg devices S_3 andS_4 are switched at medium frequency, f_m. S_5 to S_8 are the four MOSFET switches of the second inverter with body diodes D_5 to D_8 and snubber capacitors C_{S5} to C_{S8}, respectively. These inverter devices are switched at high frequency, f_h. Lossless snubber capacitors C_{S1}–C_{S8} are connected across the switching devices S_1–S_8, respectively, to provide ZVS operation. V_{dc1} and V_{dc2} are supply voltages of the first and second inverters, respectively. Three different IH resonant loads are connected across the output terminals of cascaded inverters. The output voltage of cascaded inverters is $v_o = v_{01}+v_{02}$, where v_{01} and v_{02} are the output voltages of the first and second inverters, respectively, i_o is the output current of the cascaded inverter.

This induction cooking system consists of three burners, each one suitable for iron, steel, and aluminium vessels, respectively. L_{1lf} and R_{1lf} are, respectively, the equivalent inductance and resistance of iron load at low frequency, f_l. An external capacitor C_{1r} is connected in series to resonate this load at low resonant frequency, f_{rl}. L_{2mf} and R_{2mf} are, respectively, the equivalent inductance and resistance of steel load at medium frequency, f_m. C_{2r} is the external capacitor connected in series to resonate this load at medium resonant frequency, f_{rm}. L_{3hf}, and R_{3hf} are, respectively, the equivalent inductance and resistance of aluminium load at high frequency, f_h. An external capacitor C_{3r} is connected in series to resonate this load at high resonant frequency, f_{rh}. i_{lf}, i_{mf}, and i_{hf} are the currents through iron, steel, and aluminium resonant loads, respectively. The low, medium, and high switching frequencies are selected as $f_l = 20\,\text{kHz}$, $f_m = 100\,\text{kHz}$, and $f_h = 400\,\text{kHz}$, respectively. Switching pulses of the inverter devices, corresponding output voltage v_o and load currents i_{lf}, i_{mf}, and i_{hf} are shown in Fig. 3. i_o is the sum of low, medium, and high frequency current components.

2.2 Selection of switching frequencies

The induction cooking system needs a higher frequency AC supply (≥20 kHz). Low frequency utility supply voltage (50 Hz) is converted into higher frequency voltage and applied to a induction cooker. This conversion stage consists of a bridge rectifier, filter circuit and a high-frequency inverter. The heat generated in the vessel concentrates in a peripheral layer at a skin depth (δ) of

$$\delta = \sqrt{\frac{\rho}{\pi \mu f_s}} \tag{1}$$

where ρ is the electrical resistivity and μ is the magnetic permeability of the vessel material, and f_s is the switching frequency of the inverter. Ferromagnetic materials have higher values of permeability and resistivity. The equivalent circuit of induction heating load may be considered as a series combination of L_{eq} and R_{eq}, where L_{eq} is the equivalent inductance and R_{eq} is the equivalent resistance, as referred to the IH coil side when the vessel is kept on the cooker. These values depend on the material of the vessel used are varying with a switching frequency.

In this paper, three vessels made of iron, steel, and aluminium are considered. Iron is ferromagnetic material. Steel and aluminium are non-ferromagnetic materials. The variation of L_{eq} and R_{eq} of these three different IH loads with an inverter switching frequency is shown in Fig. 4. Fig. 4*a* shows the L_{eq} and R_{eq} variation of iron load with a frequency and Figs. 4*b* and *c* show the same for steel and aluminium vessels. It is observed that iron load has higher values of L_{eq} and R_{eq} at around 20 kHz. Hence, the switching frequency, f_l of iron IH load is selected as 20 kHz. Steel and aluminium loads are having less value of L_{eq} and R_{eq} at this frequency. Beyond 80 kHz, the equivalent resistance of steel load increases above 2 Ω and similarly beyond 300 kHz equivalent resistance of aluminium increases above 2 Ω. Hence by increasing switching frequency, the equivalent resistance and thereby output power may be increased. The switching frequency of steel IH load is selected at a medium frequency of 100 kHz and that of aluminium is selected at a high frequency of 400 kHz. External capacitors are connected to IH loads to resonate the load at the resonant frequency f_r. To facilitate ZVS operation, $f_s div f_r$ ratio has to be selected closer to 1.1. Hence f_{rl}, f_{rm}, and f_{rh} are selected as 18.4, 98, and 395 kHz, respectively. The resonant capacitors are selected based on the expressions for f_{rl}, f_{rm} and f_{rh}, where

$$f_{rl} = \frac{1}{2\pi\sqrt{L_{1lf}C_{1r}}}, \quad f_{rm} = \frac{1}{2\pi\sqrt{L_{2mf}C_{2r}}} \quad \text{and} \quad f_{rh} = \frac{1}{2\pi\sqrt{L_{3hf}C_{3r}}}, \tag{2}$$

respectively.

The admittance characteristics of the three IH loads are shown in Fig. 5. It shows that the iron, steel, and aluminium resonant loads offer maximum admittance to low, medium, and high-frequency currents, respectively.

2.3 Operating principle

The output voltage of the proposed cascaded inverter v_o is the sum of first and second inverter output voltages v_{01} and v_{02}, respectively. The first inverter is operated at low and medium frequencies. The second inverter is operated at high frequency. Hence the cascaded inverter output voltage v_o is the combination of low, medium, and high frequency voltage components, v_{olf}, v_{omf}, and v_{ohf}, as shown in Fig. 3.

$$v_0 = v_{01} + v_{02} = v_{olf} + v_{omf} + v_{ohf} \tag{3}$$

Fig. 6*a* shows the equivalent circuit of inverter loads. Inverter output current waveform and its FFT are also shown. It depicts i_o as a combination of low, medium, and high frequency currents. The behaviour of loads for the low frequency component of an output voltage v_{olf} is shown in Fig. 6*b*. At low-frequency f_l, the resonant capacitors C_{2r} and C_{3r} offer very high reactance and act like an

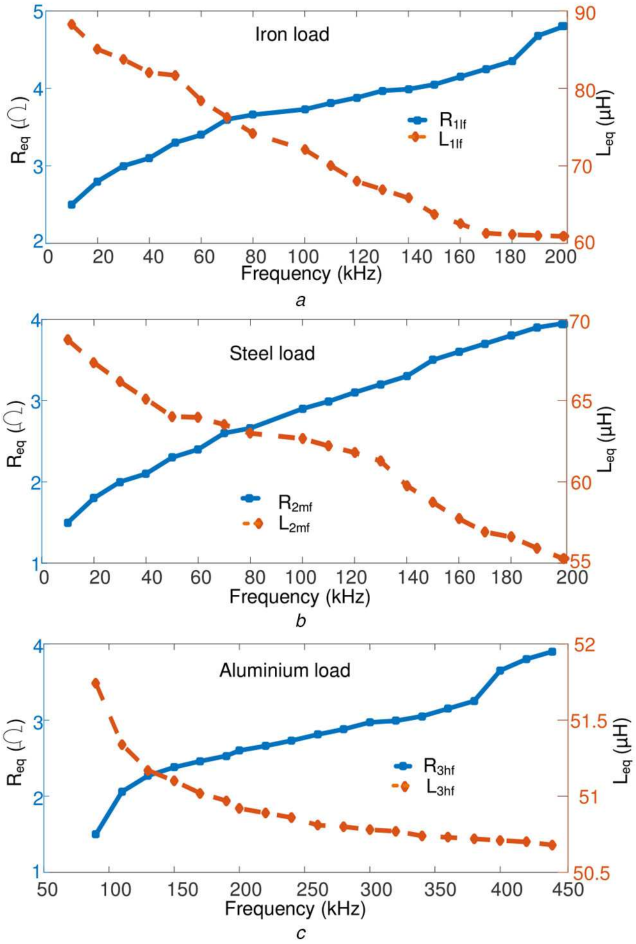

Fig. 4 *Variation of R_{eq} and L_{eq} with frequency*
(a) Iron load, ***(b)*** Steel load, ***(c)*** Aluminium load

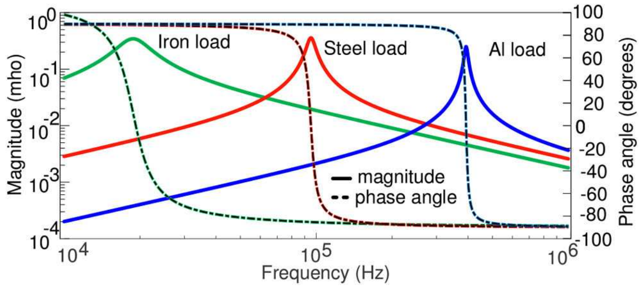

Fig. 5 *Admittance curves of different IH resonant loads*

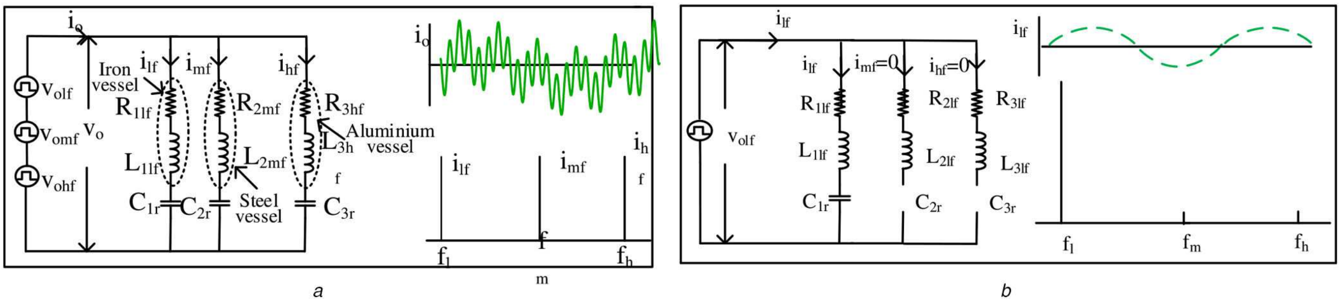

Fig. 6 *Load equivalent circuit, load currents and FFT*
(a) Operation with l_f, m_f, and h_f components, ***(b)*** Low frequency load equivalent circuit

open circuit and hence the low frequency current component i_{1lf} does not flow through medium and high frequency loads. Now the impedance of iron vessel resonant load can be expressed as

$$Z_{1lf} = R_{1lf} + j(X_{L1lf} - X_{C1lf}) \tag{4}$$

where $X_{L1lf} = 2\pi f_l L_{1lf}$, $X_{c1lf} = 1/(2\pi f_l C_{1r})$.

However, $X_{L1lf} \simeq X_{C1lf}$ and hence $Z_{1lf} \simeq R_{1lf}$. Thus, the iron resonant load provides least resistance path for i_{1lf} and it flows through the iron load. At medium frequency f_m, the inductive reactance of L_{1mf} and capacitive reactance of C_{3r} are very high and hence they behave like open circuits. At medium frequency, the steel vessel resonant load impedance can be expressed as

$$Z_{2mf} = R_{2mf} + j(X_{L2mf} - X_{C2mf}) \tag{5}$$

where X_{L2mf}=$2\pi f_m L_{2mf}$, and X_{c2mf}=$1/(2\pi f_m C_{2r})$

However, $X_{L2mf} \simeq X_{C2r}$ and hence $Z_{2mf} \simeq R_{2mf}$. Thus, the steel resonant load provides least resistance path for i_{mf} and it flows through the steel load. At high frequency f_h, the inductive reactance of L_{1hf} and capacitive reactance of L_{2hf} are very high and hence they behave like an open circuit. At high frequency, an aluminium vessel resonant load impedance can be expressed as

$$Z_{3hf} = R_{3hf} + j(X_{L3hf} - X_{C3hf}) \tag{6}$$

where X_{L3hf}=$2\pi f_h L_{3hf}$, and X_{C3hf}=$1/(2\pi f_h C_{2r})$

However, $X_{L3hf} \simeq X_{C3r}$ and hence $Z_{3hf} \simeq R_{3hf}$. Thus, the aluminium resonant load provides least resistance path for the high frequency current component i_{hf}. Hence high frequency current flows through the aluminium load.

2.3.1 Output power control: The total output power of this multi-load induction heating inverter configuration is expressed as

$$P_0 = P_{ol} + P_{om} + P_{oh} \tag{7}$$

where P_{ol} = iron load output power =$I_{lf}^2 R_{lf}$, P_{om} = steel load output power =$I_{mf}^2 R_{mf}$, and P_{oh} = alluminium load output power =$I_{hf}^2 R_{hf}$, I_{lf}, I_{mf} and I_{hf} are RMS values of iron, steel, and aluminium load currents. These output powers delivered to different vessel loads are controlled independently using asymmetric duty cycle control. P_{ol} is controlled through ADC control in the first inverter low-frequency leg devices. P_{ol} can be expressed as

$$P_{ol} = \frac{2V_{dc}^2 \cos^2\phi_l}{\pi^2 R_{1lf}} \cos^2\frac{\alpha_l}{2} \tag{8}$$

where $\phi_l = \tan^{-1}((X_{L1lf} - X_{C1lf})/R_{1lf})$, α_l = control angle, ϕ_l = phase angle.

At a fixed frequency, all parameters are constant except the control angle α_l. By varying this control angle, the low frequency duty cycle and output power P_{ol} are controlled. Similarly, the first inverter medium-frequency leg (leg-2) devices are operated with ADC. The output power P_{om} can be controlled by varying the medium-frequency control angle α_m. This output power P_{om} is expressed as

$$P_{om} = \frac{2V_{dc}^2 \cos^2\phi_m}{\pi^2 R_{2mf}} \cos^2\frac{\alpha_m}{2} \tag{9}$$

where $\phi_m = \tan^{-1}((X_{L2mf} - X_{C2mf})/R_{2mf})$.

Switching pulses of the second inverter devices S_5 and S_8 are always in phase and S_6 and S_7 are in phase. This inverter output is also controlled by α_h is the control angle. ϕ_h is the phase angle between the fundamental components of v_{hf} and i_{hf}. P_{oh} can be expressed as

$$P_{oh} = \frac{2V_{dc}^2 \cos^2\phi_h}{\pi^2 R_{3hf}} \cos^2\frac{\alpha_h}{2} \tag{10}$$

where $\phi_h = \tan^{-1}((X_{L3hf} - X_{C3hf})/R_{3hf})$, P_{oh} can be controlled by varying the high frequency control angle α_h. Thus, independent control of the individual load currents and load powers is achieved through ADC control.

3 Modes of operation

With the equal source voltages, $V_{dc1} = V_{dc2} = V_{dc}$, the inverter operation can be explained through eight different modes. When low-frequency device S_1 is ON, four operating modes are possible depending on the switching states of medium and high frequency devices. These modes are explained as below:

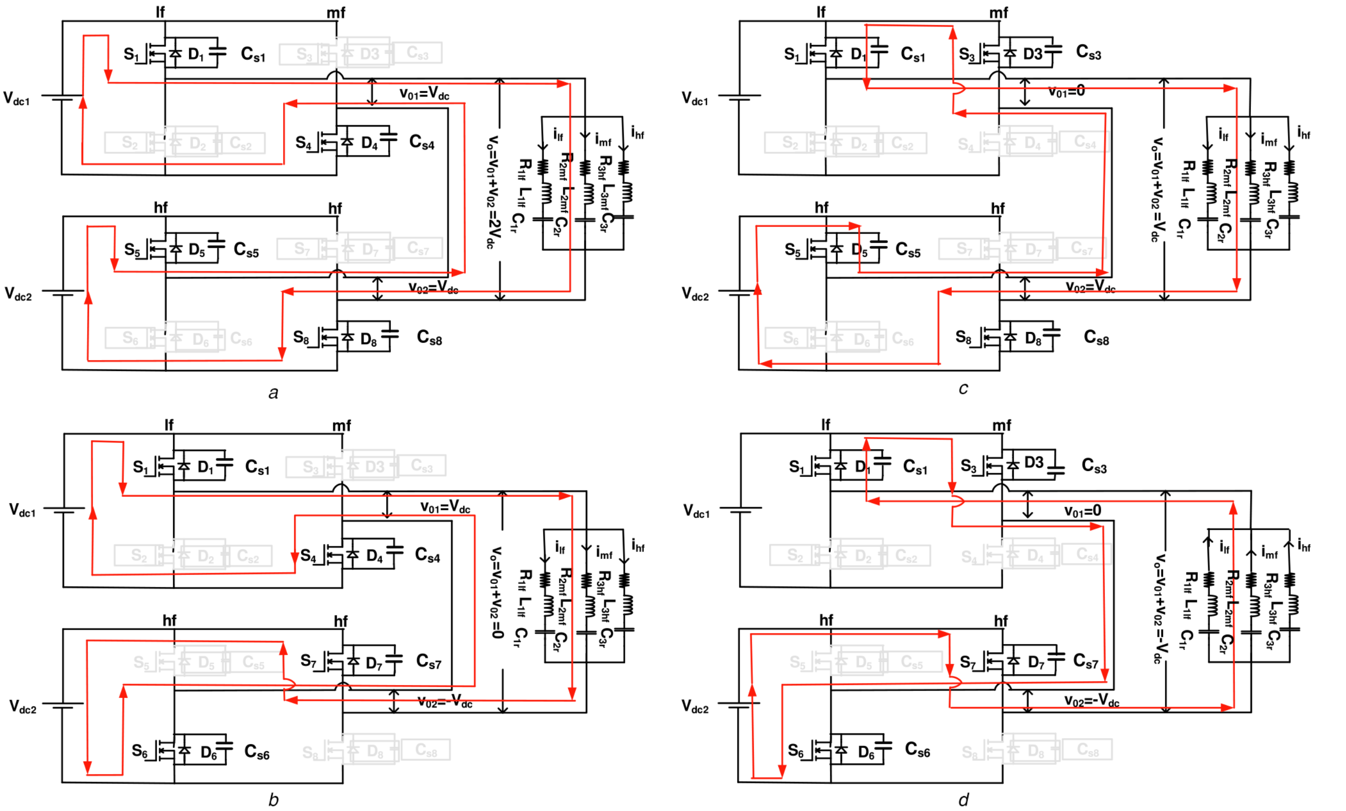

Fig. 7 *Inverter equivalent circuits for different modes of operation with S_1 is ON*
(a) Mode-1: S_1, S_4, S_5 and S_8 are ON, ***(b)*** Mode-2: S_1, S_4, S_6 and S_7 are ON, ***(c)*** Mode-3: S_1, S_3, S_5 and S_8 are ON, ***(d)*** Mode-4: S_1, S_3, S_6 and S_7 are ON

Mode-1: In this mode, switches S_1, S_4, S_5, and S_8 are in on-state. The corresponding equivalent circuit is shown in Fig. 7*a*. Output voltages of the first and second inverters are, respectively, $V_{01} = V_{dc}$ and $V_{02} = V_{dc}$. The output voltage across the loads (v_o) is the sum of V_{01} and V_{02}.

$$v_o = v_{01} + v_{02} = 2V_{dc} \quad (11)$$

the instantaneous value of inverter load current

$$i_o(t) = i_{lf}(t) + i_{mf}(t) + i_{hf}(t) \quad (12)$$

Mode-2: In this mode, switches S_1, S_4, S_6, and S_7 are in on-state. The corresponding equivalent circuit is shown in Fig. 7*b*. Output voltages of the first and second inverters are, respectively, $V_{01} = V_{dc}$ and $V_{02} = -V_{dc}$. Output voltage across the loads is expressed as

$$v_o = v_{01} + v_{02} = 0 \quad (13)$$

Mode-3: In this mode, switches S_1, S_3, S_5 and S_8 are in on-state. The corresponding equivalent circuit is shown in Fig. 7*c*. Output voltages of the first and second inverters are, respectively, $V_{01} = 0$ and $V_{02}= V_{dc}$. The output voltage across the loads is expressed as

$$v_o = v_{01} + v_{02} = V_{dc} \quad (14)$$

Mode-4: In this mode, switches S_1, S_3, S_6 and S_7 are in on-state. The corresponding equivalent circuit is shown in Fig. 7*d*. Output voltages of the first and second inverters are, respectively, $V_{01} = 0$ and $V_{02} = -V_{dc}$. The output voltage across the loads is expressed as

$$v_o = v_{01} + v_{02} = -V_{dc} \quad (15)$$

When S_2 is ON, more four operating modes are possible as explained below:
Mode-5: In this mode, switches S_2, S_3, S_6, and S_7 are in on-state. Output voltages of the first and second inverters are, respectively, $V_{01} = -V_{dc}$ and $V_{02} = -V_{dc}$. The output voltage across the loads is expressed as

$$v_o = v_{01} + v_{02} = -2V_{dc} \quad (16)$$

Mode-6: In this mode, switches S_2, S_3, S_5 and S_8 are in on-state. Output voltages of the first and second inverters are, respectively, $V_{01} = -V_{dc}$ and $V_{02} = V_{dc}$. The output voltage across the loads is expressed as

$$v_o = v_{01} + v_{02} = 0 \quad (17)$$

Mode-7: In this mode switches S_2, S_4, S_6, and S_7 are in on state. Output voltages of the first and second inverters are, respectively, $V_{01} = 0$ and $V_{02} = -V_{dc}$. The output voltage across the loads is expressed as

$$v_o = v_{01} + v_{02} = -V_{dc} \quad (18)$$

Mode-8: In this mode switches S_2, S_4, S_5, and S_8 are in on state. Output voltages of the first and second inverters are, respectively, $V_{01} = 0$ and $V_{02} = V_{dc}$. Output voltage across the loads is expressed as

$$v_o = v_{01} + v_{02} = V_{dc} \quad (19)$$

4 Simulation and experimental results

A 150 W prototype of the cascaded resonant inverter has been implemented for three different material vessel induction-cooking applications. The circuit parameters are presented in Table 1. Two isolated, equal DC voltage sources of $V_{dc1} = 30$ V and $V_{dc2} = 30$ V are used. The IH load parameters are measured from the coil side with the different material vessels of iron, steel, and aluminium are kept over respective IH coils. Iron, steel, and aluminium vessels, which are most commonly used in cooking applications, are selected for experimentation. These different vessel loads are resonated at frequencies of 18.4, 98, and 395 kHz, respectively, with corresponding switching frequencies of 20, 100, and 400 kHz, respectively. The ADC control is used for independent control of each load power.

Fig. 8 shows the simulation and experimental waveforms corresponding to equal duty cycles of D_l=0.95, D_m=0.95, and D_h =0.95. Fig. 8*a* shows the simulation waveforms of load voltage,

Table 1 Experimental prototype parameters

Parameter	Value
DC voltage source-1 (V_{dc1})	30 V
DC voltage source-2 (V_{dc2})	30 V
iron vessel equivalent inductance at low frequency (L_{1lf})	88.6 μH
iron vessel equivalent resistance at low frequency (R_{1lf})	2.87 Ω
resonant capacitor at low frequency (C_{1r})	0.96 μF
steel vessel equivalent inductance at medium frequency (L_{2mf})	62.45 μH
steel vessel equivalent resistance at medium frequency (R_{2mf})	2.9 Ω
resonant capacitor at medium frequency (C_{2r})	0.044 μF
aluminium vessel equivalent inductance at high frequency (L_{3hf})	50.7 μH
aluminium vessel equivalent resistance at high frequency (R_{3hf})	3.6 Ω
high frequency vessel resonant capacitor (C_{3r})	0.321 nF
low switching frequency (f_l)	20 kHz
iron load resonant frequency (f_{rl})	18.5 kHz
medium switching frequency (f_m)	100 kHz
steel load resonant frequency (f_{rm})	98 kHz
high switching frequency (f_h)	400 kHz
aluminium load resonant frequency (f_{rh})	398 kHz
MOSFETs used	IRFB4227pbf
$R_{DS(on)}$	19 mΩ
DSP controller	TMS320F28379D

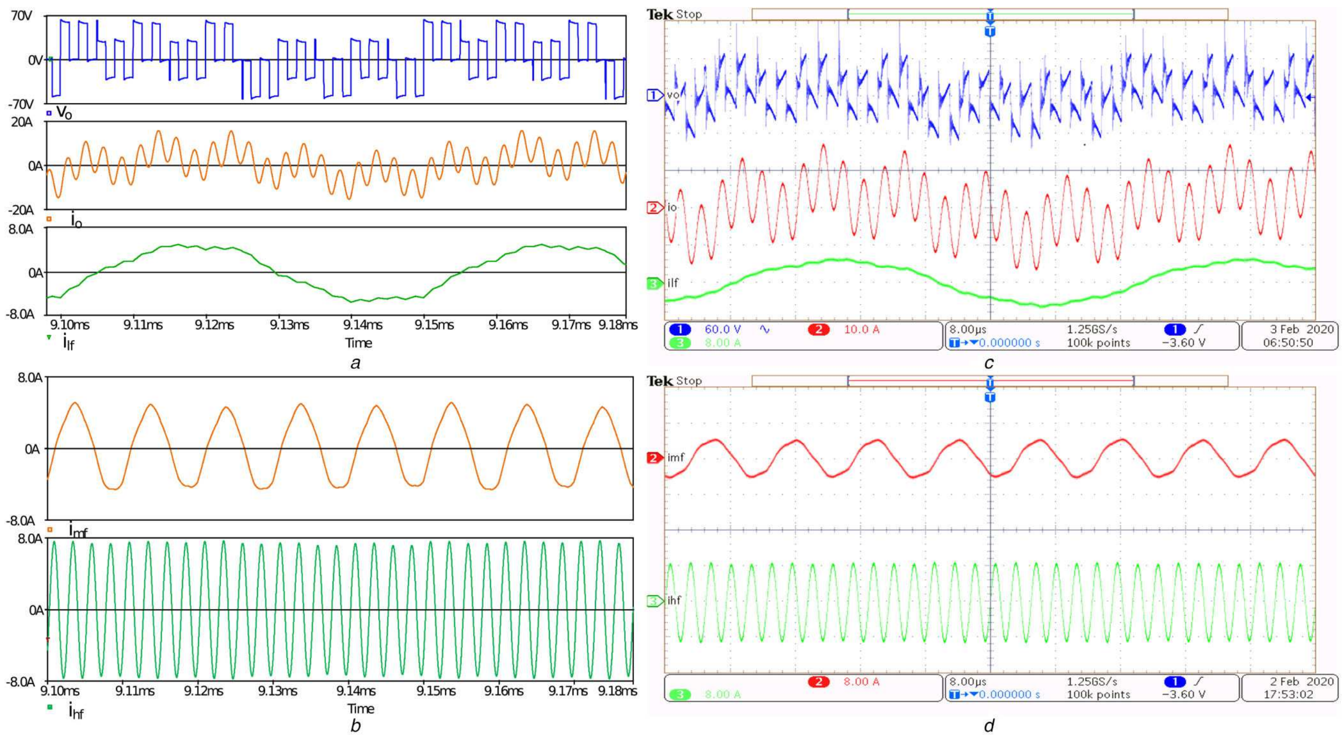

Fig. 8 *Load voltage (v_o), inverter output current (i_o) and load currents at D_l=0.95, D_m=0.95 and D_h=0.95*

(a) Simulated waveforms of v_o, i_o and i_{lf}, ***(b)*** Simulated waveforms of i_{mf} and i_{hf}, ***(c)*** Experimental waveforms of v_o, i_o and i_{lf}, ***(d)*** Experimental waveforms of i_{mf} and i_{hf}

inverter output current, and low-frequency current. Fig. 8*b* shows the simulation waveforms of medium and high-frequency load currents. Figs. 8*c* and *d* show the corresponding experimental waveforms. Figs. 9*a* and *b* show, respectively, FFTs of simulated and experimental inverter output current at D_l=0.95, D_m=0.95, and D_h=0.95. It is observed that this current contains only the low, medium, and high frequency components with RMS values of I_{lf} =3 A, I_{mf}=3.2 A, and I_{hf}=4.72 A. It is also observed that the experimental and simulation results are in good agreement with each other. (Fig. 10) shows the simulation and experimental waveforms corresponding to duty cycles of D_l=0.2, D_m=0.95 and D_h=0.95. Fig. 10*a* shows the simulation waveforms of load voltage, inverter output current, and low-frequency current, Fig. 10*b* shows the simulation waveforms of medium and high-frequency load currents. Figs. 10*c* and *d* show the corresponding experimental waveforms. Figs. 11*a* and *b* show, respectively, FFTs of simulated and experimental inverter output current at D_l=0.2, D_m=0.95 and D_h=0.95. It is observed that the low-frequency load current is reduced to I_{lf}=1.7 A, whereas medium and high frequency load currents remain at the same values of I_{mf}=3.2 A and I_{hf}=4.72 A. This indicates independent load control, as the reduction in low-frequency duty cycle, decreases only low-frequency load current, whereas the other load currents remain unaffected. It is also observed that the experimental and simulation results are in good

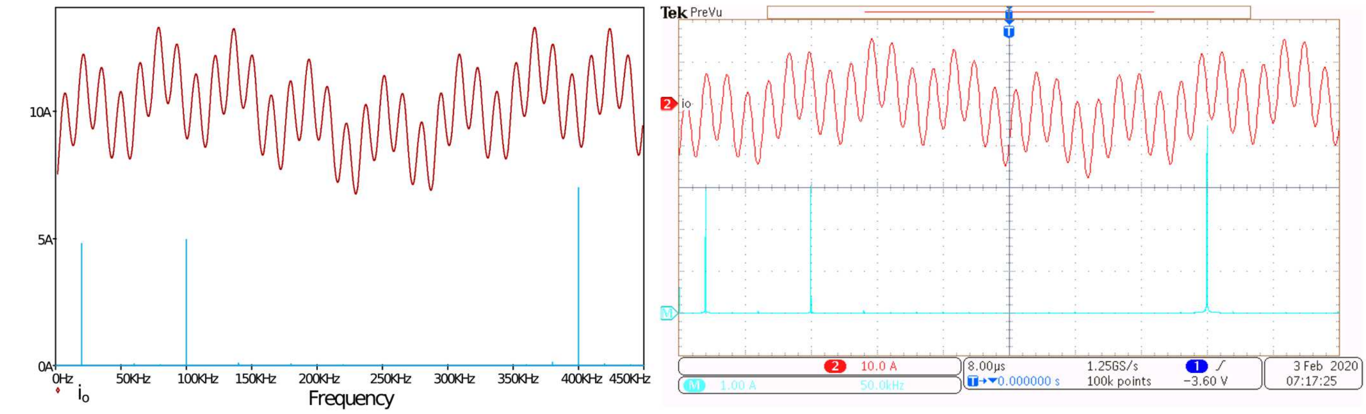

a *b*

Fig. 9 *Inverter output current i_o and its FFT at D_l=0.95, D_m=0.95 and D_h=0.95*

(a) Simulated waveforms, ***(b)*** experimental waveforms

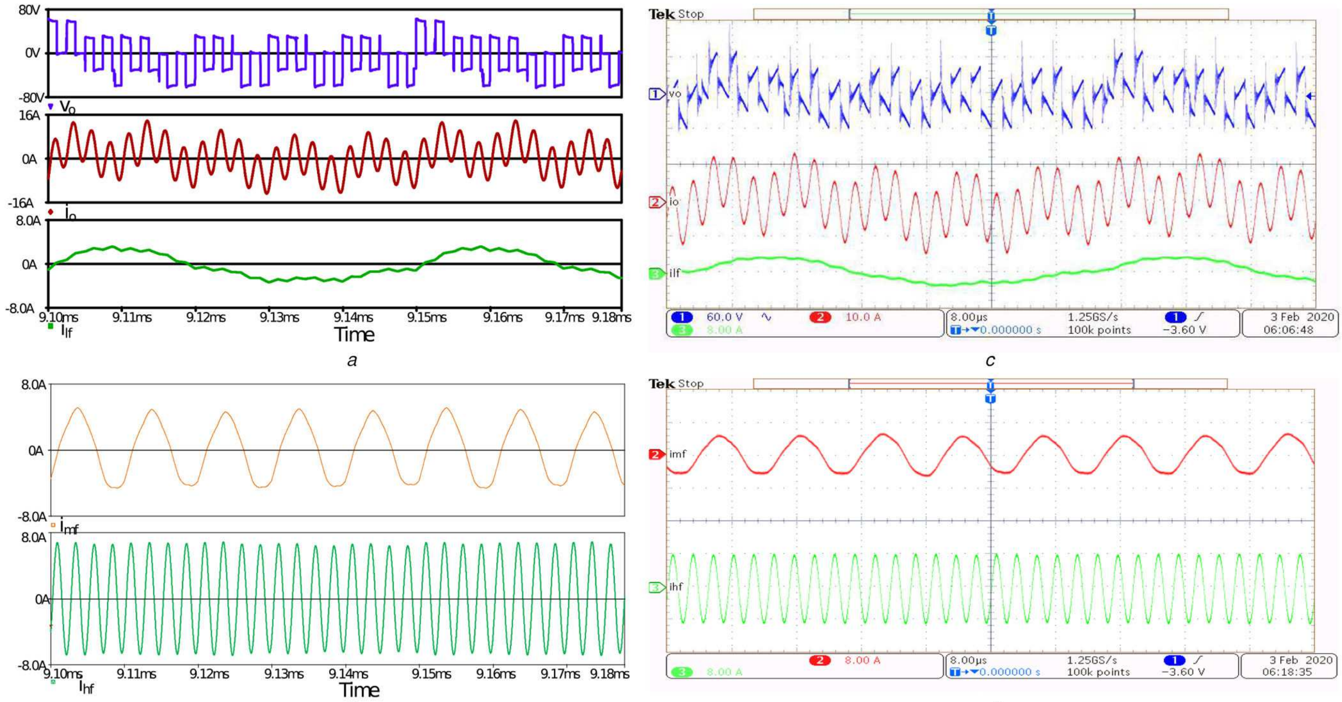

a *c* *b* *d*

Fig. 10 *Load voltage (v_o), inverter output current (i_o) and load currents at D_l=0.2, D_m=0.95, and D_h=0.95*

(a) Simulated waveforms of v_o, i_o, and i_{lf}, ***(b)*** Simulated waveforms of i_{mf} and i_{hf}, ***(c)*** Experimental waveforms of v_o, i_o, and i_{lf}, ***(d)*** Experimental waveforms of i_{mf} and i_{hf}

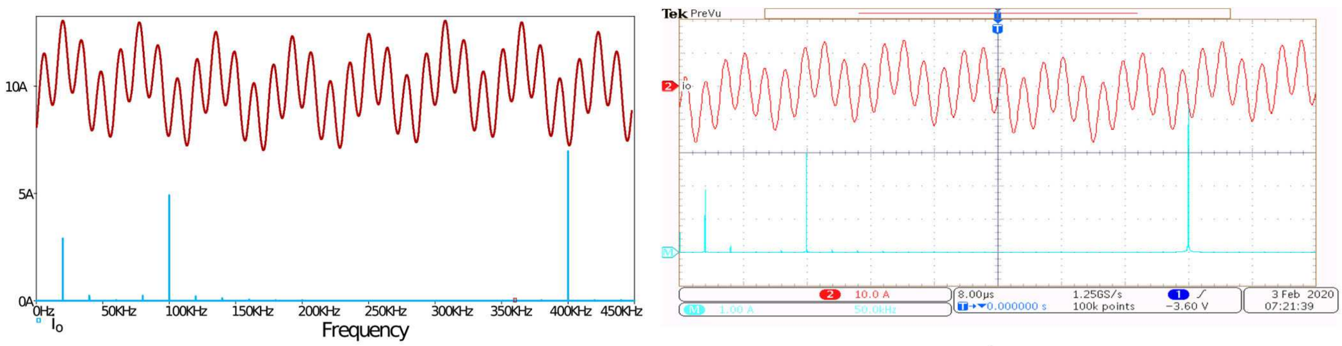

a *b*

Fig. 11 *Inverter output current i_o and its FFT at D_l=0.2, D_m=0.95, and D_h=0.95*

(a) Simulated waveforms, ***(b)*** Experimental waveforms

agreement with each other. Fig. 12 shows the simulation and experimental waveforms corresponding to duty cycles of D_l=0.95, D_m=0.2, and D_h=0.95. Fig. 12*a* shows the simulation waveforms of load voltage, inverter output current, and low-frequency current. Fig. 12*b* shows the simulation waveforms of medium and high frequency load currents. Figs. 12*c* and *d* show the corresponding experimental waveforms. Figs. 13*a* and *b* show, respectively, FFTs of simulated and experimental inverter output currents at D_l=0.95, D_m=0.2, and D_h=0.95. It is observed that the medium frequency load current is reduced to I_{mf}=1.8 A, whereas low and high-

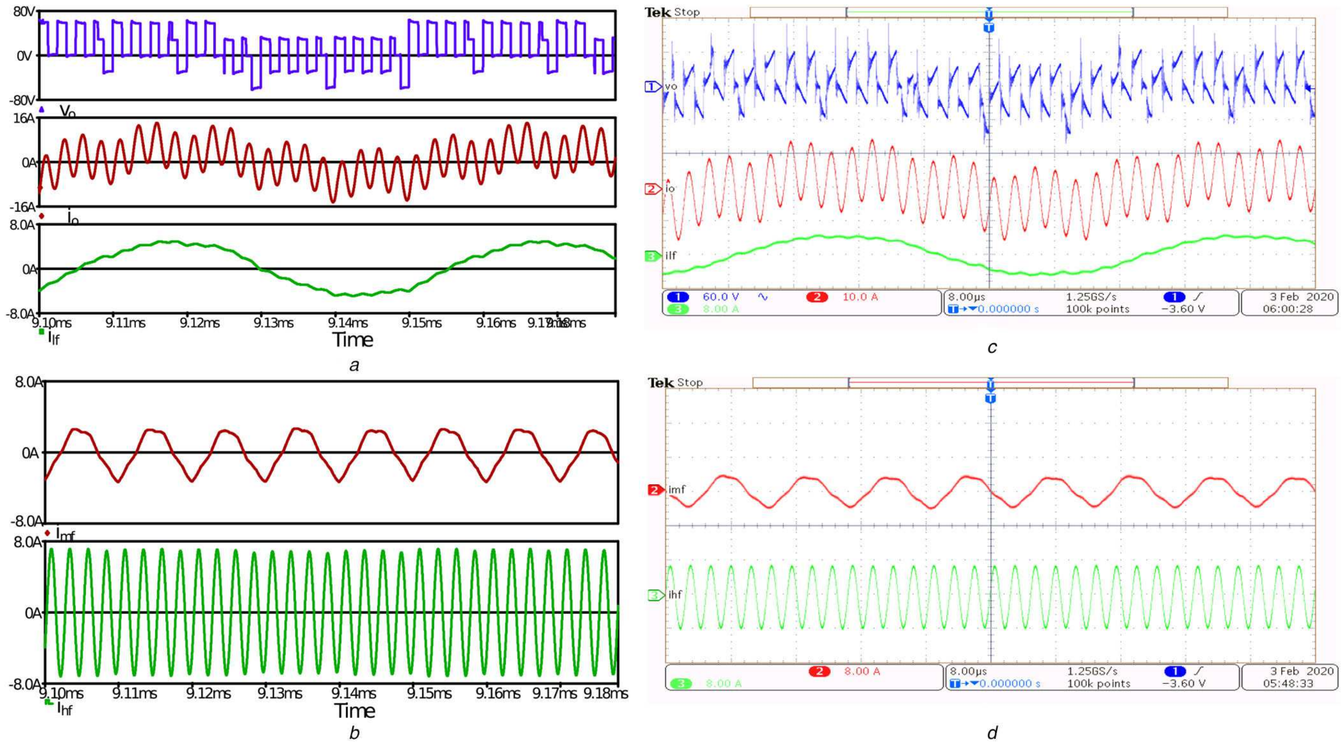

Fig. 12 *Load voltage (v_o), inverter output current (i_o) and load currents at D_l=0.95, D_m=0.2, and D_h=0.95*

(a) Simulated waveforms of v_o, i_o, and i_{lf}, ***(b)*** Simulated waveforms of i_{mf}, and i_{hf}, ***(c)*** Experimental waveforms of v_o, i_o, and i_{lf}, ***(d)*** Experimental waveforms of i_{mf} and i_{hf}

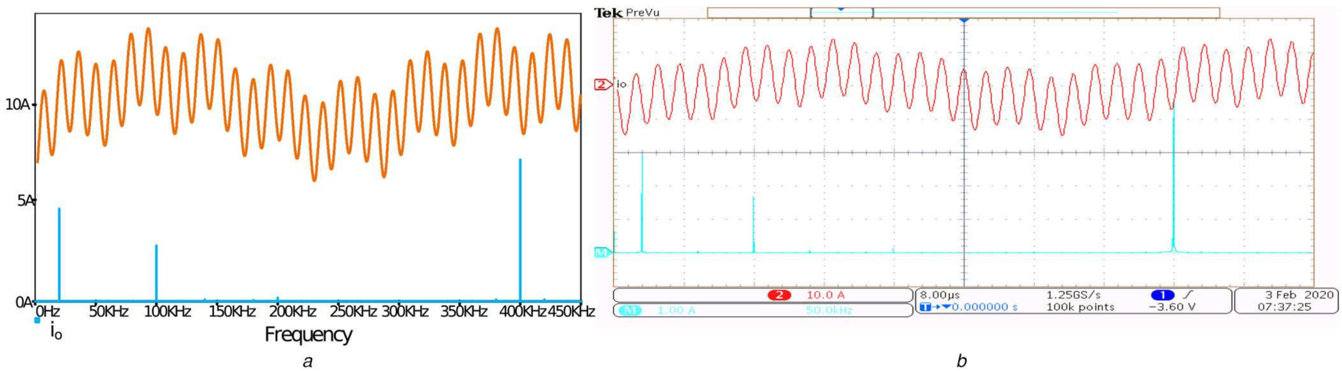

Fig. 13 *Inverter output current i_o and its FFT at D_l=0.95, D_m=0.2, and D_h=0.95*

(a) Simulated waveforms, ***(b)*** Experimental waveforms

frequency load currents remain at the same values of I_{lf}=3A and I_{hf}=4.72 A. This indicates independent load control and it is also observed that the experimental and simulation results are in good agreement with each other. Fig. 14 shows the simulation and experimental waveforms corresponding to duty cycles of D_l=0.95, D_m=0.95, and D_h=0.2. Fig. 14*a* shows simulation waveforms of load voltage, inverter output current, and low-frequency current. Fig. 14*b* shows simulation waveforms of medium and high frequency load currents. Figs. 14*c* and *d* show the corresponding experimental waveforms. Figs. 15*a* and *b* show, respectively, FFTs of simulated and experimental inverter output currents at D_l=0.95, D_m=0.95, and D_h=0.2. It is observed that the high-frequency load current is reduced to I_{hf}=2 A, whereas low and medium-frequency load currents remain at the same values of I_{lf}=3 A and I_{mf}=3.2 A. This indicates independent load control and it is observed that the experimental and simulation results are in good agreement with each other.

5 Analysis of results

In the proposed multi-IH load cascaded inverter, power control is realised through ADC control. The experimental setup is shown in Fig. 16. Based on the thermal measurement, the temperature variations in different vessels are shown in Fig. 17. From the simulation and experimental results, the output powers of individual loads have been calculated as described in Section 2.3.1. The load power variation with the ADC control is shown in Fig. 18. Fig. 18*a* shows the variation of load powers P_{ol}, P_{om}, and P_{oh} with low-frequency duty cycle (D_l) when D_m and D_h are kept constant at 0.95. Now it can be observed that only iron vessel load power (P_{ol}) is varying while other load powers remain constant. Simulation and experimental results are in good agreement with each other. Fig. 18*b* shows the variation of load powers with medium-frequency duty cycle (D_m) when D_l and D_h are kept constant at 0.95. It can be observed that only steel vessel load power (P_{om}) is varying while other load powers remain constant. Simulation and experimental results are in good agreement with each other. Fig. 18*c* shows the variation of load powers with a high-frequency duty cycle (D_h) when D_l and D_m are kept constant at 0.95. It is observed that only aluminium vessel load power (P_{oh}) is varying while other load powers remain constant. Simulation and experimental results are in good agreement with each other. Hence, independent control of power in iron vessel, steel vessel, and aluminium vessel loads is verified. The total output power (P_o) of the cascaded inverter is the sum of different load powers as

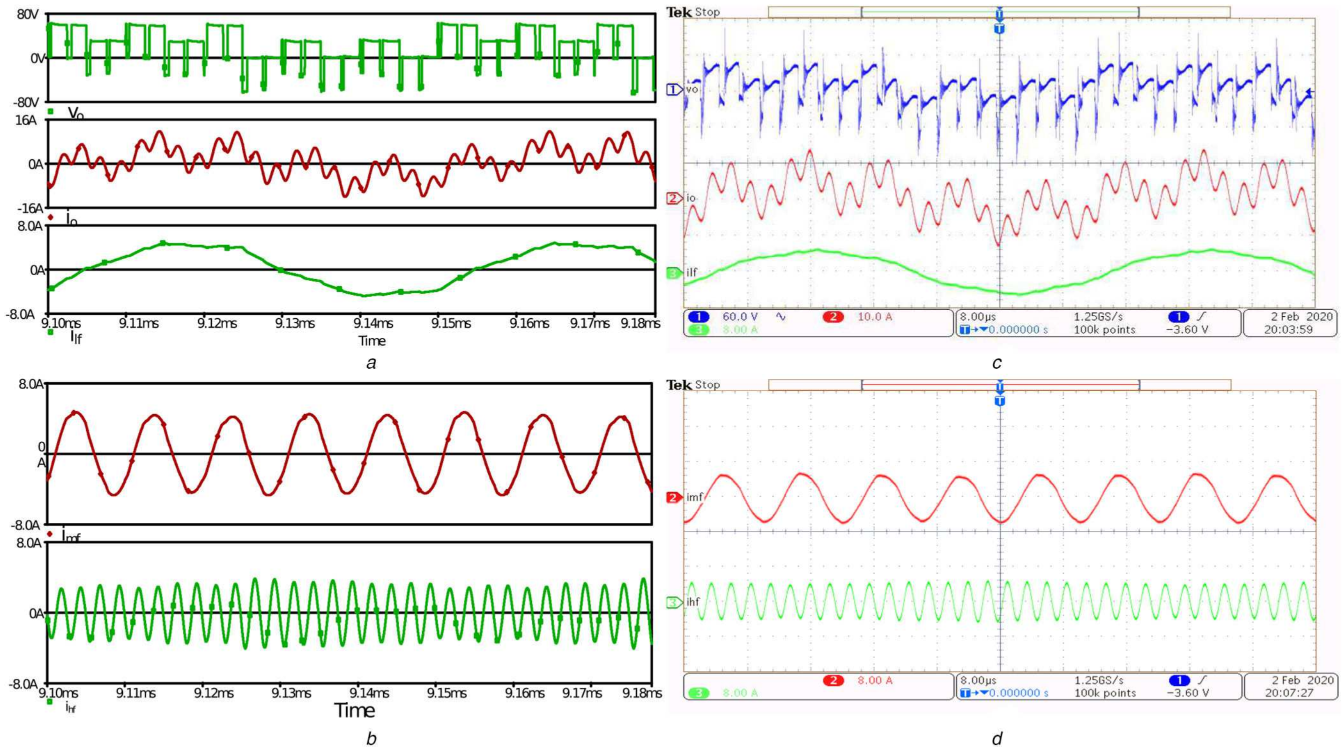

Fig. 14 *Load voltage (v_o), inverter output current (i_o) and load currents at D_l=0.95, D_m=0.95, and D_h=0.2*

(a) Simulated waveforms of v_o, i_o and i_{lf}, ***(b)*** Simulation waveforms of i_{mf} and i_{hf}, ***(c)*** Experimental waveforms of v_o, i_o and i_{lf}, ***(d)*** Experimental waveforms of i_{mf} and i_{hf}

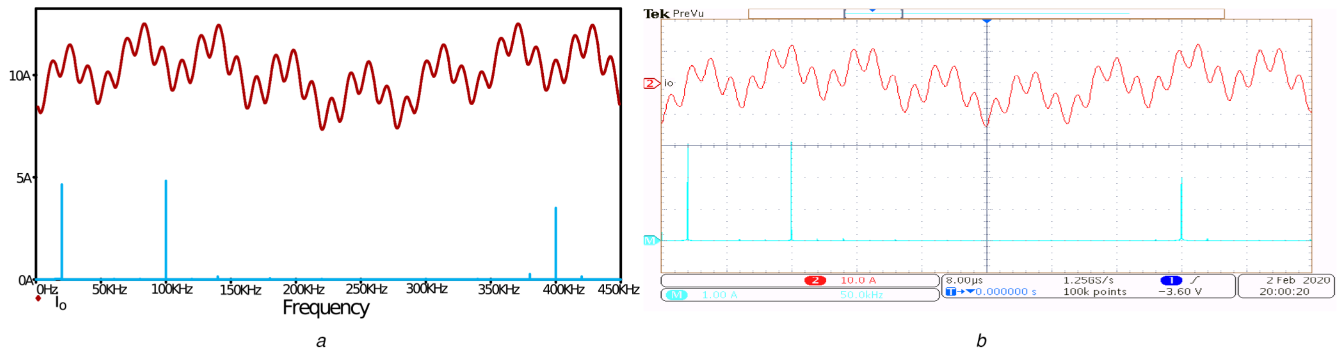

Fig. 15 *Inverter output current i_o and its FFT at D_l=0.95, D_m=0.95, and D_h=0.2*

(a) Simulated waveforms, ***(b)*** Experimental waveforms

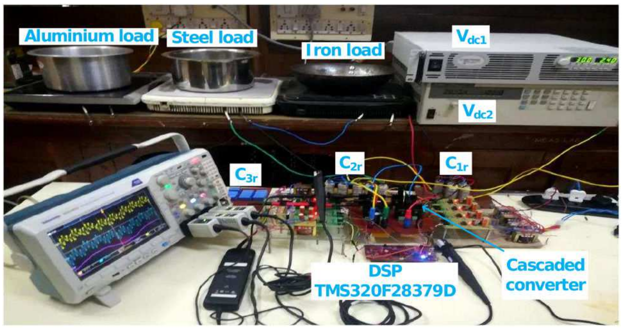

Fig. 16 *Experimental prototype*

explained. The input power of the cascaded inverter is calculated as below:

$$P_{\text{in}} = V_{\text{dc1}} I_{\text{dc1}} + V_{\text{dc2}} I_{\text{dc2}} \tag{20}$$

where I_{dc1} and I_{dc2} are the input currents of inverter-1 and inverter-2, respectively.

The overall efficiency of the cascaded inverter is calculated as

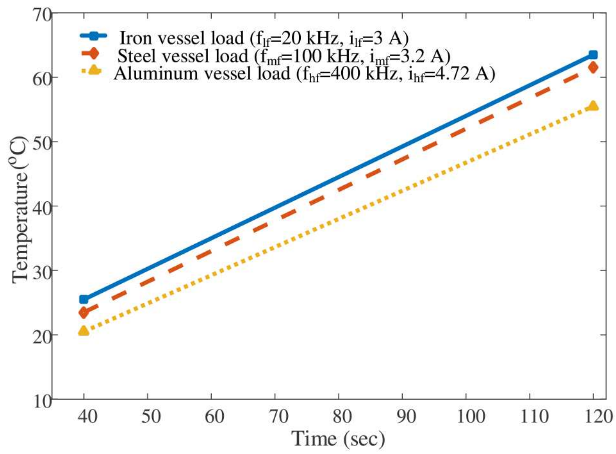

Fig. 17 *Temperature variation in different vessels*

$$\eta = \frac{P_{\text{o}}}{P_{\text{in}}} \tag{21}$$

The efficiency curves are shown in Fig. 19. Fig. 19*a* shows the graph of overall efficiency versus low-frequency duty cycle (D_l)

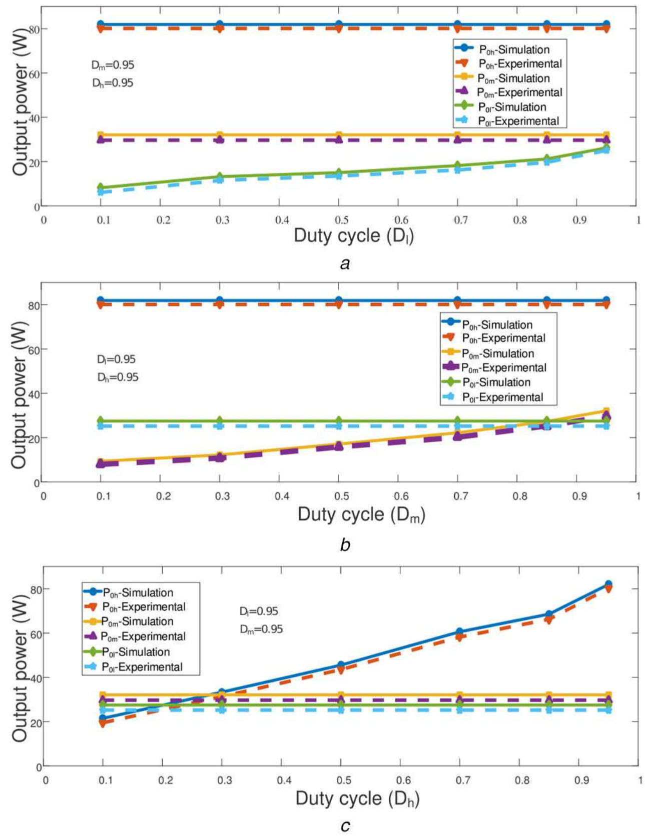

Fig. 18 *Low, medium, and high-frequency current and power control*
(a) Iron vessel power control against D_l, ***(b)*** Steel vessel power control against D_m, ***(c)*** Aluminium vessel power control against D_h

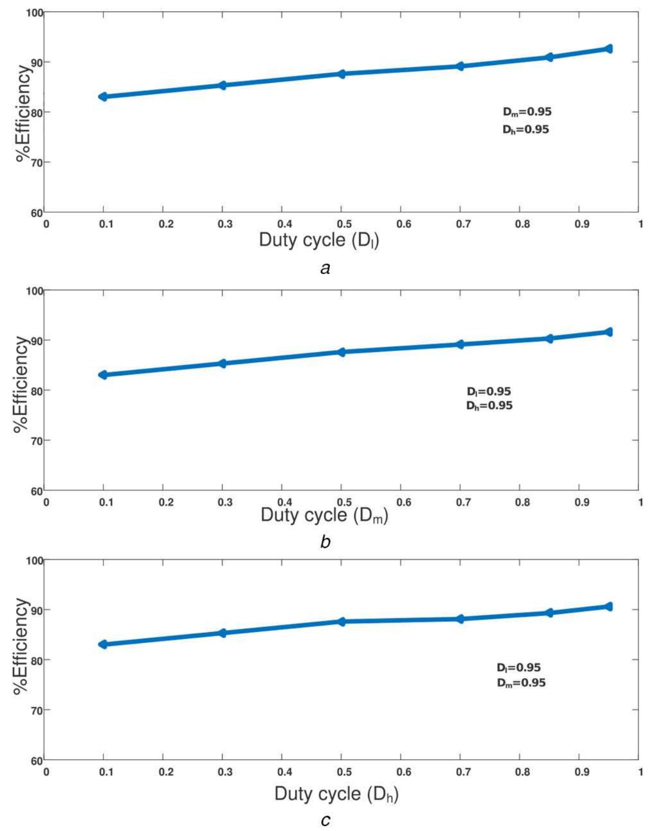

Fig. 19 *Efficiency curves*
(a) Overall efficiency versus D_l, ***(b)*** Overall efficiency versus D_m, ***(c)*** Overall efficiency versus D_h

when D_m and D_h are kept constant at 0.95. Fig. 19*b* shows the graph of overall efficiency versus medium-frequency duty cycle (D_m) when D_l and D_h are kept constant at 0.95. Fig. 19*c* shows the graph of overall efficiency versus high-frequency duty cycle (D_h) when D_l and D_m are kept constant at 0.95. From these plots, it can be observed that the overall efficiency increases with the duty cycle of the loads and vary from 85 to about 92%.

6 Conclusions

In this paper, a multi-load cascaded full-bridge resonant inverter topology is proposed for different material vessel IH loads. The first inverter legs are operated at low and medium frequencies suitable for iron and steel vessels. The second inverter is operated at high frequency suitable for aluminium vessel. Frequencies of 20, 100, and 400 kHz are used. Independent power control is achieved using asymmetric duty cycle control. The proposed inverter topology is designed, simulated and hardware prototypes are implemented.

Efficiency ≥92% is achieved at full load. This topology provides advantages of compatibility with ferromagnetic and non-ferromagnetic material vessels, independent load power control and high efficiency.

7 Acknowledgement

The authors would like to thank Central Power Research Institute (CPRI), Bangalore, India, for supporting this research work through the grant under the Research Scheme on Power (RSOP/2019/GD/12), sanctioned to Dr. S. Porpandiselvi.

8 References

[1] Plumed, E., Acero, J., Lope, I., *et al.*: 'Design methodology of high performance domestic induction heating systems under worktop', *IET Power Electron.*, 2020, **13**, pp. 300–306

[2] Lucía, O., Maussion, P., Dede, E.J., *et al.*: 'Induction heating technology and its applications: past developments, current technology, and future challenges', *IEEE Trans. Ind. Electron.*, 2013, **61**, (5), pp. 2509–2520

[3] Meng, L., Cheng, K.W.E., Chan, K.W.: 'Systematic approach to high-power and energy-efficient industrial induction cooker system: circuit design, control strategy, and prototype evaluation', *IEEE Trans. Power Electron.*, 2011, **26**, (12), pp. 3754–3765

[4] Shenkman, A., Axelrod, B., Berkovich, Y.: 'Improved modification of the single-switch ac-ac converter for induction heating applications', *IEE Proc., Electr. Power Appl.*, 2004, **151**, (1), pp. 1–4

[5] Koertzen, H.W., Van-Wyk, J.D., Ferreira, J.A.: 'Design of the half-bridge, series resonant converter for induction cooking'. Proc. of PESC'95-Power Electronics Specialist Conf., Atlanta, GA, USA, 1995, vol. 2, pp. 729–735

[6] Kazimierczuk, M.K., Jutty, M.K.: 'Fixed-frequency phase-controlled full-bridge resonant converter with a series load', *IEEE Trans. Power Electron.*, 1995, **10**, (1), pp. 9–18

[7] Ahmed, S.M.W., Eissa, M., Edress, M., *et al.*: 'Experimental investigation of full bridge series resonant inverters for induction-heating cooking appliances'. 2009 4th IEEE Conf. on Industrial Electronics and Applications, Xi'an, People's Republic of China, 2009, pp. 3327–3332

[8] Ogiwara, H., Itoi, M., Nakaoka, M.: 'Pwm-controlled soft-switching sepp high-frequency inverter for induction-heating applications', *IEE Proc., Electr. Power Appl.*, 2004, **151**, (4), pp. 404–413

[9] Kwon, Y.S., Yoo, S.B., Hyun, D.S.: 'Half-bridge series resonant inverter for induction heating applications with load-adaptive pfm control strategy'. Fourteenth Annual Applied Power Electronics Conf. and Exposition. 1999 Conf. Proc. (Cat. No. 99CH36285) (APEC'99), Dallas, TX, USA, vol. 1, 1999, pp. 575–581

[10] Burdio, J.M., Barragan, L.A., Monterde, F., *et al.*: 'Asymmetrical voltage-cancellation control for full-bridge series resonant inverters', *IEEE Trans. Power Electron.*, 2004, **19**, (2), pp. 461–469

[11] Ahmed, T., Ogura, K., Chandhaket, S., *et al.*: 'Asymmetrical duty cycle controlled edge resonant soft switching high frequency inverter for consumer electromagnetic induction fluid heater', *Automatica, ATKAAF*, 2003, **44**, (1-2), pp. 21–26

[12] Mishima, T., Sakamoto, S., Ide, C.: 'Zvs phase-shift pwm-controlled single-stage boost full-bridge ac–ac converter for high-frequency induction heating applications', *IEEE Trans. Ind. Electron.*, 2016, **64**, (3), pp. 2054–2061

[13] Shen, J., Ma, H., Yan, W., *et al.*: 'PDM and PSM hybrid power control of a series-resonant inverter for induction heating applications'. 2006 1ST IEEE Conf. on Industrial Electronics and Applications, Singapore, Singapore, 2006, pp. 1–6

[14] Forest, F., Labouré, E., Costa, F., *et al.*: 'Principle of a multi-load/single converter system for low power induction heating', *IEEE Trans. Power Electron.*, 2000, **15**, (2), pp. 223–230

[15] Burdio, J.M., Monterde, F., Garcia, J.R., *et al.*: 'A two-output series-resonant inverter for induction-heating cooking appliances', *IEEE Trans. Power Electron.*, 2005, **20**, (4), pp. 815–822

[16] Vijaya.Bhaskar, D., Vishwanathan, N., Maity, T., Porpandiselvi, S.: 'A three-output inverter for induction cooking application with independent control', *EPE J.*, 2018, **28**, (2), pp. 89–99

[17] Papani, S.K., Neti, V., Murthy, B.K.: 'Dual frequency inverter configuration for multiple-load induction cooking application', *IET Power Electron.*, 2015, **8**, (4), pp. 591–601

[18] Sarnago, H., Lucia, O., Mediano, A., *et al.*: 'Design and implementation of a high-efficiency multiple-output resonant converter for induction heating applications featuring wide bandgap devices', *IEEE Trans. Power Electron.*, 2013, **29**, (5), pp. 2539–2549

[19] Lucia, O., Carretero, C., Burdio, J.M., *et al.*: 'Multiple-output resonant matrix converter for multiple induction heaters', *IEEE Trans. Ind. Appl.*, 2012, **48**, (4), pp. 1387–1396

[20] Hirokawa, T., Okamoto, M., Hiraki, E., *et al.*: 'A novel type time-sharing high-frequency resonant soft-switching inverter for all metal ih cooking appliances'. 37th Annual Conf. of the IEEE Industrial Electronics Society (IECON 2011), Melbourne, VIC, Australia, 2011, pp. 2526–2532

[21] Hirokawa, T., Hiraki, E., Tanaka, T., *et al.*: 'The practical evaluations of time-sharing high-frequency resonant soft-switching inverter for all metal ih cooking appliances'. 38th Annual Conf. on IEEE Industrial Electronics Society (IECON 2012), Montreal, QC, Canada, 2012, pp. 3302–3307

[22] Yonemori, H., Kobayashi, M.: 'On the heating characteristic and magnetic flux of a double-coil drive type induction heating cooker'. 32nd Annual Conf. on IEEE Industrial Electronics (IECON 2006), Paris, France, 2006, pp. 2488–2493

[23] Han, W., Chau, K., Jiang, C., *et al.*: 'All-metal domestic induction heating using single-frequency double-layer coils', *IEEE Trans. Magn.*, 2018, **54**, (11), pp. 1–5

[24] Millan, I., Burdío, J., Acero, J., *et al.*: 'Series resonant inverter with selective harmonic operation applied to all-metal domestic induction heating', *IET Power Electron.*, 2011, **4**, (5), pp. 587–592

[25] Park, H.P., Jung, J.H.: 'Load-adaptive modulation of a series-resonant inverter for all-metal induction heating applications', *IEEE Trans. Ind. Electron.*, 2018, **65**, (9), pp. 6983–6993

[26] Shuvo, S., Hossain, E., Islam, T., *et al.*: 'Design and hardware implementation considerations of modified multilevel cascaded h-bridge inverter for photovoltaic system', *IEEE Access*, 2019, **7**, pp. 16504–16524

[27] Wang, Y., Du, G., Liang, J., *et al.*: 'Flexible cascaded multilevel inverter with multiple operation modes', *J. Power Electron.*, 2020, **20**, pp. 675–686

[28] Choudhary, R., Suryawanshi, H.M., Talapur, G.G., *et al.*: 'Modified cascaded multi-level inverter structure with reduced voltage stress across h-bridge for high voltage application', *Electr. Power Compon. Syst.*, 2018, **46**, (6), pp. 659–672

[29] Liu, J., Cheng, K., Ye, Y.: 'A cascaded multilevel inverter based on switched-capacitor for high-frequency ac power distribution system', *IEEE Trans. Power Electron.*, 2013, **29**, (8), pp. 4219–4230

[30] Corzine, K., Familiant, Y.: 'A new cascaded multilevel h-bridge drive', *IEEE Trans. Power Electron.*, 2002, **17**, (1), pp. 125–131

[31] Shalini, B.A.P., Sethuraman, S.: 'Cascaded multilevel inverter for industrial applications'. Int. Conf. on Advances in Information Technology and Mobile Communication, Berlin, Heidelberg, Germany, 2012, pp. 339–344

[32] Li, Y., Mai, R., Yang, M., *et al.*: 'Cascaded multi-level inverter based ipt systems for high power applications', *J. Power Electron.*, 2015, **15**, (6), pp. 1508–1516

[33] Diong, B., Basireddy, S., Corzine, K., *et al.*: 'Multilevel inverters with equal or unequal sources for dual-frequency induction heating'. Nineteenth Annual IEEE Applied Power Electronics Conf. and Exposition (APEC'04), Roanoke, VA, USA, 2004, vol. 2, pp. 825–831

[34] Diong, B., Basireddy, S., Corzine, K.: 'Multilevel converter-based dual-frequency induction heating power supply'. 29th Annual Conf. of the IEEE Industrial Electronics Society (IEEE Cat. No. 03CH37468) (IECON'03),vol. 2, Anaheim, CA, USA, 2003, pp. 1992–1997

[35] Qingfeng, L., Huamin, W., Zhaoxia, L.: 'Discuss on the application of multilevel inverter in high frequency induction heating power supply'. 2006 IEEE Region 10 Conf. (TENCON 2006), Hong Kong, People's Republic of China, 2006, pp. 1–4

[36] Porpandiselvi, S., Vishwanathan, N.: 'Inverter configuration for simultaneous dual frequency induction hardening with independent control', *EPE J.*, 2013, **23**, (1), pp. 13–20